

Non-Planar Coil Winding Angle Optimization for Compatibility with Non-Insulated High-Temperature Superconducting Magnets

C. Paz-Soldan¹

General Atomics, San Diego, California 92186-5608, USA^{a)}

(Dated: 28 October 2021)

The rapidly emerging technology of high-temperature superconductors (HTS) opens new opportunities for the development of non-planar non-insulated HTS magnets. This type of HTS magnet offers attractive features via its simplicity, robustness, and is well-suited for modest size steady-state applications such as a mid-scale stellarator. In non-planar coil applications the HTS tape may be subject to severe minor-axis bending strain (ϵ_{bend}), torsional strains (ϵ_{tor}) and transverse magnetic field components (B_{\perp}), all of which can limit the magnet operating space. A novel method of winding angle optimization is here presented to overcome these limitations. Essentially, this method: 1) calculates the peak ϵ_{bend} and B_{\perp} for arbitrary winding angle along an input coil filamentary trajectory, 2) defines a cost function including both, and then 3) uses tensioned splines to define a winding angle that reduces ϵ_{tor} and optimizes the ϵ_{bend} and B_{\perp} cost function. As strain limits are present even without B_{\perp} , this optimization is able to provide an assessment of the minimum buildable size of an arbitrary non-planar non-insulating HTS coil. This optimization finds that for standard 4 mm wide HTS tapes the minimum size coils of the existing HSX, NCSX, and W7-X stellarator geometries are around 0.3 - 0.5 m in radius. For coils larger than this size, permitting a finite (yet tolerable) strain allows reduction of B_{\perp} . This enables a reduction of the HTS tape length required to achieve a given design magnetic field or equivalently an increase in the achievable magnetic field for fixed HTS tape length. The distinct considerations for optimizing a stellarator coilset to further ease compatibility with non-insulated HTS magnets are also discussed.

I. INTRODUCTION AND MOTIVATION

High-temperature superconductors (HTS) have been recognized for the past two decades to offer attractive new pathways for magnet development¹. Compared to low-temperature superconductors (LTS), HTS enables the design of magnets that operate either at higher magnetic field, higher temperature, higher current density, or combinations of all three. Compared to copper, HTS (and LTS) offers the benefit of significantly reduced energy dissipation within the magnet, enabling continuous operation at higher magnetic field. Naturally, these attributes of HTS are opening new opportunities for applications that benefit from improved magnets²⁻⁵. Robust efforts are ongoing to deploy HTS technology toward large-bore high-field magnets for magnetic fusion energy applications^{6,7}.

While worldwide focus has been largely directed towards high-field planar magnet systems, little attention has been paid to new opportunities enabled by HTS in applications that benefit from improved non-planar magnets. Non-planar configurations can be found in force-balanced (helical) coils for magnetic energy storage⁸, particle accelerator magnets using saddle/bedstead⁹ or canted cosine theta¹⁰ geometries, and the stellarator concept of a magnetic fusion energy system^{11,12}.

The unusual (essentially 2D) form factor of HTS tape has given rise to several methods to convert the tape into a viable conductor. Integrated multi-tape conduc-

tor concepts include: interleaving HTS tapes into a Roebel assembly¹³, winding HTS tape helically along a cylindrical form (termed Cable on Round Core, CORC conductor¹⁴), and forming stacks of many HTS tape layers and winding the stack in various arrangements (termed twisted stacked-tape conductor¹⁵). However, the first and still the simplest method to construct a magnet from HTS tape is simply to wind the HTS tape in a ‘bare’ non-insulated and non-epoxy impregnated configuration around a bobbin that defines the shape of the final coil. This type of coil is referred to as a non-insulated HTS coil (NI-HTS)^{16,17}.

A. Primer on Benefits and Drawbacks of Uninsulated HTS Magnets

A central benefit of the NI-HTS magnet is its simplicity. In this configuration the HTS tape is wound directly onto a shaped bobbin that defines the winding geometry, and the desired performance (in kiloamp turns, kAt) is achieved simply by adding turns. These coils do not require (and indeed cannot allow) cooling channels within the conductor stack. Any heat generated must instead be rejected through the bobbin structure. Also, as the number of turns in the NI-HTS magnet is generally very large, a low supply current (and thus a low input power) is required to drive them.

Beyond simplicity, owing to the absence of an insulator between turns, NI-HTS magnets offer a degree of intrinsic superconductivity quench protection, as the electrical current is offered a multitude of parallel paths to avoid the non-superconducting failure point¹⁸. Finally, as the

^{a)}Electronic mail: paz-soldan@fusion.gat.com

HTS tape itself consists of superconducting layers deposited onto a steel substrate, winding an NI-HTS tape magnet on a steel bobbin results in a final assembly mechanically very similar to pure steel. This yields reduced differential thermal expansion issues and significantly enhanced strength as compared to other magnets.

Drawbacks can also be identified. Owing to the large number of turns of conductor (N) required, NI-HTS coils are typically high in inductance ($L \propto N^2$) and thus cannot change current quickly unless large voltages are utilized. This makes NI-HTS coils challenging to use in AC operation modes. This often limits deployment to truly steady-state applications, such as long-timescale energy storage, particle accelerators, and the stellarator fusion concept. Notably, NI-HTS would be challenging to use in the poloidal field coils of the tokamak fusion concept due to the time-varying current requirement.

The NI-HTS coil also suffers from a second drawback. For large-bore, high-field applications, the number of turns required is very large, as is the path length of each turn. Either severely long lengths of HTS tape or a large number of resistive joints are thus required, creating a practical limitation to the ultimate potential of this magnet type. These drawbacks naturally drive development towards the complex multi-tape conductor assemblies as described earlier.

B. Compatibility of Uninsulated HTS Magnets with Non-Planar Applications

Considering deployment of NI-HTS magnets to non-planar applications, two additional constraints arise. First, the radius of curvature along the winding trajectory no longer points towards a fixed point, but instead can take arbitrary form. This necessitates the introduction of *wrong-ways bending* strain and *torsional bending* strain. Secondly, the magnetic field generated by the magnet is no longer predominantly parallel to the HTS tape plane (as it is in a planar magnet), but instead has significant transverse field components (B_{\perp}). Both of these issues degrade the HTS tape performance and ultimately limit its operating space.

In this work a new winding angle optimization method is developed and presented to mitigate the aforementioned HTS tape compatibility issues of strain and transverse field. The winding angle is a free parameter for any filamentary coil model, and will here be exploited as an optimization parameter to mitigate the issues associated with deploying NI-HTS coils in non-planar applications.

C. Goal, Structure, and Summary of Work

The goal of this paper is to discuss the compatibility of NI-HTS coils for non-planar applications and to present a novel winding angle optimization method developed to overcome the identified limitations. The optimization

method is described in Sec. II, and the candidate non-planar coil geometries examined (well-known stellarator designs) are described in Sec. III. Results of strain-only optimizations are presented in Sec. IV. These optimizations are able to assess the minimum size of a non-planar coil that can be wound without exceeding strain limits for a given width of HTS tape, which are found to be 0.3 - 0.5 m radius for the studied stellarator configurations. Results of combined strain and B_{\perp} optimizations are presented in Sec. V. By defining coils larger than the minimum size, headroom is created to allow reduction of the B_{\perp} component, enabling access to higher field for fixed tape HTS length, or the same field at reduced HTS tape length. The degree of benefit depends on the target coil size, as this method can quantify. Conclusions are presented in Sec. VI along with a discussion of how to optimize the coil geometry itself for improved compatibility with NI-HTS magnets.

II. WINDING ANGLE OPTIMIZATION METHOD

By calculating the peak strain due to minor-axis bending (ϵ_{bend}) along with B_{\perp} along the coil trajectory as a function of winding angle (θ_{wind}), a trajectory can be found that minimizes arbitrary cost functions of these two metrics. To minimize torsional strain (ϵ_{tor}) a tensioned spline fit to the optimal trajectory allows identification of the optimum trade-off between the cost function and ϵ_{tor} . Each of these steps is now described in detail.

A. Strain Considerations

Two strain components are possibly severe in non-planar coils made with NI-HTS tape, as illustrated in Fig. 1. These are the minor-axis bending strain (ϵ_{bend}) and the torsional strain (ϵ_{tor})¹⁹.

The minor-axis bending strain is linearly proportional to the distance along the HTS tape width, and the magnitude depends on the radius of curvature via the following simple relationship:

$$\epsilon_{bend}(x) = \frac{x}{|r_C|}, \quad (1)$$

where r_C is the radius of curvature, and x is the position along the tape width w . It peaks at $x = w/2$, the tape edge, with a value of $\epsilon_{bend} = w/2|r_C|$. Here r_C is calculated numerically using finite differences²⁰, though if the coil trajectory is parametrized it can also be described analytically using the Frenet-Serret formulas²¹.

Note the major-axis bending strain is also given by a similar relation, but it is smaller by the ratio of the tape width to its thickness. As normal HTS tape widths are 4, 6, and 12 mm while thicknesses are 0.1 mm, this strain component can be safely ignored. This also means that as long as the radius of curvature is directed along the major

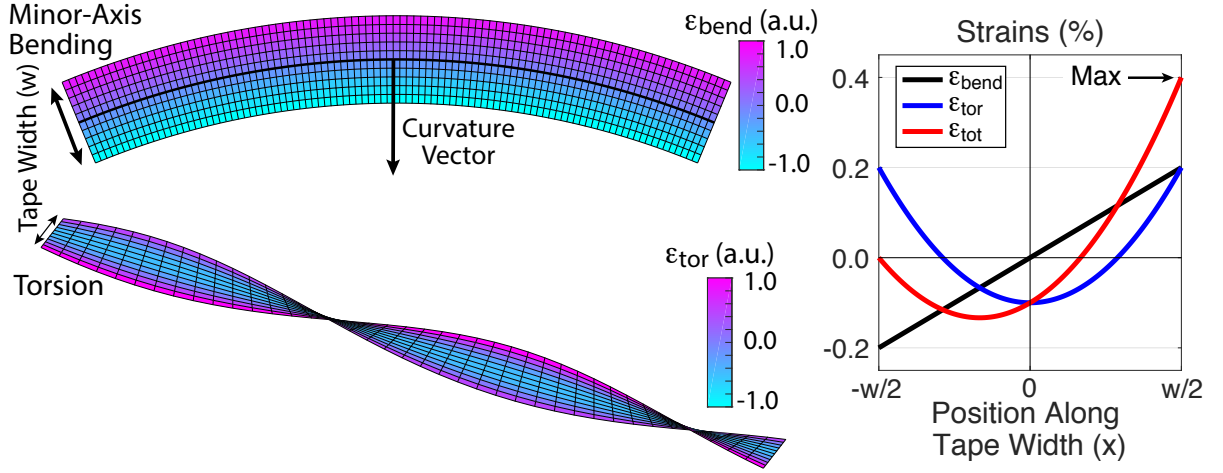


FIG. 1. Visualization of the strain components considered in the optimization. The minor-axis bending strain (ϵ_{bend} , top-left) is linearly proportional to the distance along the HTS tape width, while the torsional strain (ϵ_{tor} , bottom-left) takes a offset-parabolic form. The peak strain (ϵ_{tot}) is simply found by summing these two components, and it is always found at one edge of the HTS tape.

axis of the tape, a 40x-120x smaller radius of curvature can be tolerated. This can greatly impact optimization of the coil trajectory itself as will be discussed separately in Appendix A. Note major-axis strain is ignored in this study because it is so much lower than minor-axis strain.

The torsional strain (ϵ_{tor}) does not depend on the local radius of curvature but instead is related to the angular rate of change of r_C along the coil trajectory. The torsional strain takes the form¹⁹:

$$\epsilon_{tor}(x) = \frac{1}{2} \left(\frac{\Delta\theta_{wind}}{\Delta L} \right)^2 \left(x^2 - \frac{w^2}{12} \right) \quad (2)$$

for a position x along the tape width w , where $\Delta\theta$ is the angular rate of change of the winding angle θ_{wind} per unit length along the coil trajectory (ΔL). ϵ_{tor} takes an offset-parabolic form and also peaks at the tape edge ($x = \pm w/2$), with a value of $\epsilon_{tor} = (\Delta\theta_{wind}/\Delta L)^2 w^2/12$. $\Delta\theta_{wind}$ is also calculated numerically using finite differences, but it too can be described analytically using the Frenet-Serret formulas if the trajectory is parametrized.

A scalar metric representing the total strain ($\equiv \epsilon_{tot}$) is now defined from ϵ_{bend} and ϵ_{tor} . To rigorously treat the problem, the three-dimensional internal strains at every point in the tape should be taken into account using the Principle Strain Method (PSM)²², including actual material properties such as the Poisson Ratio, Modulus of Elasticity, and Modulus of Rigidity to relate the different strain tensor elements. To simplify the problem and avoid sensitivity to material properties, a less rigorous but more conservative metric is used in this work - the maximum of a scalar sum of the ϵ_{bend} and ϵ_{tor} components:

$$\epsilon_{tot} = \max(\epsilon_{bend}(x) + \epsilon_{tor}(x)). \quad (3)$$

Note the maximum ϵ_{tot} always occurs at one tape edge or another ($x = \pm w/2$), based on the relative directions

of ϵ_{bend} and ϵ_{tor} . This method is conservative because it assumes the strain components are fully co-linear (which is approximately true in the limit of thin tapes). Comparison of Eq. 3 and the PSM finds the strain can be over-estimated by 15-20% by Eq. 3. This over-estimate is expected to be compensated by increases in the real material strain introduced by material imperfections, giving additional credence to this conservative approach.

In terms of a limit to the acceptable ϵ_{tot} , in principle empirical data should be gathered at the target operating strain and field conditions to validate the expected performance of the HTS tape. In the absence of such data this study uses an industry rule-of-thumb, which is that a maximum ϵ_{tot} limit of 0.4% should be enforced^{23,24}. Above this limit there is a risk of reduction in the critical superconducting current I_{crit} capacity as well as delamination of the internal layers within the HTS tape²⁵. Regardless, the optimization framework can take arbitrary strain limits as input, and results are generally given in terms of peak predicted ϵ_{tot} .

B. Transverse Field Considerations

While strain is the primary consideration as exceeding its limit has more severe consequences, a secondary consideration is the transverse magnetic field (B_{\perp}). This imposes a soft limit on HTS tape performance as increasing B_{\perp} also degrades I_{crit} . For this study, data on this limitation is obtained from publicly available HTS tape manufacturer data²⁶.

Note that unlike the strains, B_{\perp} depends on coils throughout the entire configuration. As such to compute B_{\perp} the fields from all conductors in the configuration must be taken into account. This includes all other magnets as well as the fields from other turns within the

magnet. A limitation of the present study is that the cross-sectional geometry of the conductor is not defined, as such the B_{\perp} from finite coil winding pack aspect ratio is not presently treated. This limitation may be improved upon in the future.

C. Optimization Philosophy and Cost Function Definition

As the ϵ_{bend} limit is a hard constraint on the HTS integrity, while B_{\perp} is a softer limit, the optimization philosophy is thus to first ensure strain is within tolerable limits, and then within these limits to optimize against B_{\perp} as a secondary constraint. Since ϵ_{bend} and B_{\perp} are single-valued functions of the winding angle θ_{wind} , they can be directly computed for all possible θ_{wind} . This is shown in Fig. 2(b) for a single point along an example coil trajectory (the coil geometries considered will be described in Sec. III). As can be seen, ϵ_{bend} depends sensitively on HTS tape width, while B_{\perp} naturally depends on the coil current. As can also be seen, the optimal θ_{wind} to minimize B_{\perp} and ϵ_{bend} are different. Aligning θ_{wind} to the local curvature ensures $\epsilon_{bend}=0$, noting this can be achieved on either the bobbin effective outer diameter (O.D.) or inner diameter (I.D.).

The method chosen to enable simultaneous optimization of ϵ_{bend} and B_{\perp} is to define a cost function that is a linear sum of ϵ_{bend} and B_{\perp} with an ad-hoc relative scale-factor α :

$$Cost = \begin{cases} \epsilon_{bend} + \alpha B_{\perp} & \text{if } \epsilon_{bend} > \epsilon_0 \\ \epsilon_0 + \alpha B_{\perp} & \text{if } \epsilon_{bend} < \epsilon_0 \end{cases} \quad (4)$$

The parameter ϵ_0 is the bending strain that is deemed to be tolerable and is an input free parameter. An essential feature of the cost function is that when ϵ_{bend} is below ϵ_0 the cost function sees no variation arising from ϵ_{bend} . An example cost function as applied to the same coil configuration is shown in Fig. 2(c). As can be seen, as long as the relative scale factor $\alpha \ll \max(B_{\perp})/\max(\epsilon_{bend})$, the B_{\perp} term will only have an effect when $\epsilon_{bend} < \epsilon_0$, as desired. If B_{\perp} considerations are ignorable, setting $\alpha = 0$ results in a cost function equal to only ϵ_{bend} .

D. Torsion Optimization via Tensioned Splines

Definition of a cost function to optimize θ_{wind} is not sufficient to solve the optimization problem, as the actual θ_{wind} trajectory itself impacts the total strain via the torsional strain ϵ_{tor} . This is because ϵ_{tor} is related to the rate of change of θ_{wind} along the trajectory. To address this problem, the approach is to compute the cost function across all possible θ_{wind} at all positions along the coil trajectory. This gives rise to contour plots of the cost function that visualizes the optimization prob-

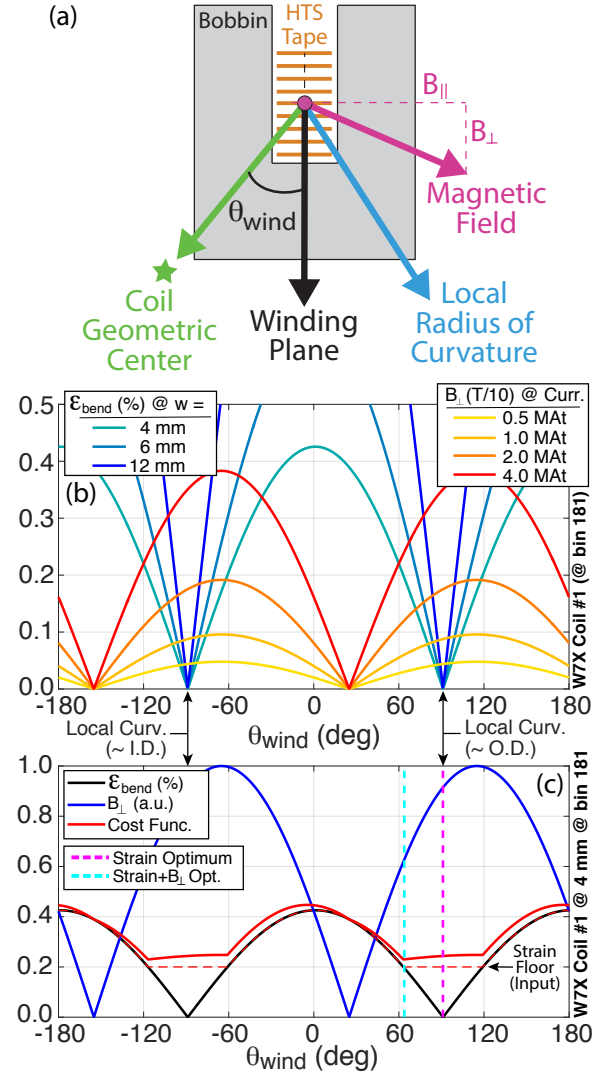


FIG. 2. (a) Cartoon illustration of a NI-HTS coil and example orientations of the winding angle (θ_{wind}), the magnetic field direction, and the local radius of curvature. Note θ_{wind} is defined relative to the coil geometric center. (b) Example evaluations of the minor-axis bending strain (ϵ_{bend}) and transverse field (B_{\perp}) as a function of θ_{wind} , with minima of each occurring for different θ_{wind} . ϵ_{bend} depends on HTS tape width while B_{\perp} depends on the coil current. If θ_{wind} is aligned to the local curvature then $\epsilon_{bend}=0$. (c) Construction of a cost function (Eq. 4) allowing B_{\perp} to be reduced while maintaining ϵ_{bend} below an input tolerable strain floor ϵ_0 . Solutions exist on both the bobbin effective outer diameter (O.D.) and inner diameter (I.D.).

lem, and provides a graphical method to reduce ϵ_{tor} while minimally increasing the cost function.

To simply illustrate this step of the optimization process a ϵ_{bend} -only cost function ($\alpha = 0$ in Eq. 4) is used, and only a subset of the coil trajectory is shown in Fig. 3. As can be seen, the contours in Fig. 3(a) are simply ϵ_{bend} contours along the coil trajectory for all possible θ_{wind} . The final θ_{wind} is fit to the minimum of the cost function

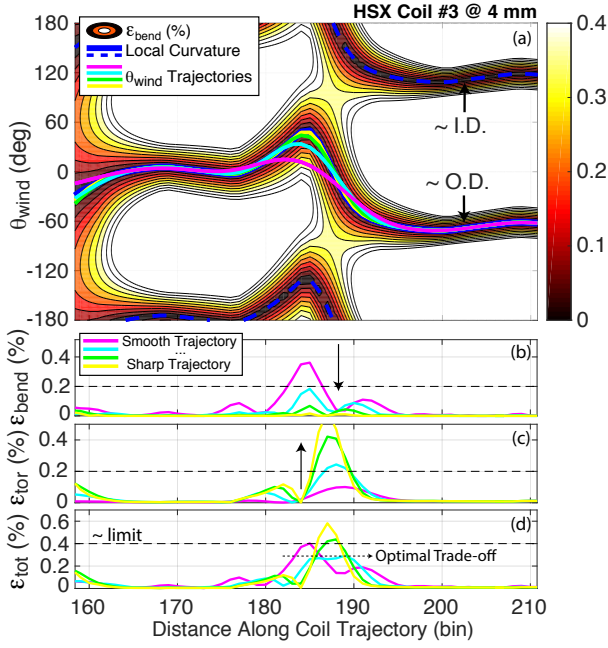


FIG. 3. Example use of spline tension to minimize total strain. (a) The cost function (here ϵ_{bend}) is plotted for all winding angles (θ_{wind}) for a subset of an example coil trajectory. Varying the spline tension yields various possible θ_{wind} trajectories. (b-d) These different trajectories trade off ϵ_{bend} and ϵ_{tor} differently, giving rise to an optimum in the total strain (ϵ_{tot}).

(the minimum of ϵ_{bend} in Fig. 3 using a tensioned spline approach. The magnitude of the local radius of curvature is used as a fitting weight for the tensioned spline, with low curvature regions ascribed a low weight. Additionally, manual adjustment of the fit is possible by inserting points with high weighting to the fitting. This can drive the fit to find alternate optimal paths through the winding trajectory. Different fitted trajectories of θ_{wind} are indicated as the colored lines in Fig. 3, with different tensions for each. For low spline tension, the fit closely matches the cost function minimum, while for high tension the variation of θ_{wind} along the coil trajectory is minimized. As can be seen in Fig. 3(b)-(d), this allows a direct tradeoff between ϵ_{bend} and ϵ_{tor} , and enables a minimum ϵ_{tot} ($=\epsilon_{bend}+\epsilon_{tor}$) to be identified. Note in some instances the optimal θ_{wind} trajectory includes regions where winding is primarily on the inner diameter of the coil ($\theta_{wind} \approx 180^\circ$), as opposed to the outer diameter ($\theta_{wind} \approx 0^\circ$).

While this method is surely not a unique solution to the optimization problem, the simple treatment is found to be sufficiently flexible to achieve the desired reduction in B_\perp within allowable ϵ_{bend} constraints.

At this point a key difference between this method and the method of calculating space-preserving maps²¹, giving rise to developable surfaces (also called the constant-perimeter method) should be clarified. As a result of the tensioned spline method utilized here, the optimal winding angle θ_{wind} does not necessarily follow the ra-

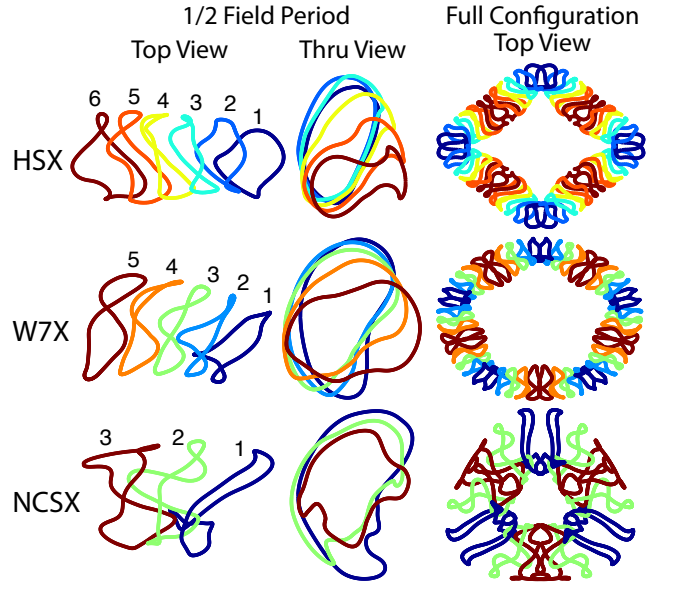


FIG. 4. Stellarator geometries considered in this study. Non-planar coils in these configurations span from weakly to strongly non-planar.

dius of curvature. As such the final tape surface is *not an area-preserving map*, and indeed this is why finite ϵ_{bend} is present. Were an area-preserving map method map utilized, the resultant trajectory would likely undergo severe ϵ_{tor} as a result of its inability to trade off ϵ_{tor} with ϵ_{bend} , as is done here. Also to be noted is that the optimization workflow also can treat a planar coil, in which case the optimal θ_{wind} returns zero throughout as expected.

III. STELLARATOR COIL CONFIGURATIONS CONSIDERED

Though the optimization methods described in Sec. II are applicable to arbitrary coil geometry, well-known yet complex coil geometries from the stellarator are used as examples. The configurations studied are the Helically Symmetric Experiment (HSX)²⁷, the Wendelstein 7-X (W7-X) stellarator^{28,29}, and the National Compact Stellarator Experiment (NCSX)^{30,31}. Each coilset was generated primarily based on varying constraints arising from plasma physics, alongside engineering constraints from the coilsets. Note that each configuration differs in physical size and magnet technology (HSX and NCSX are copper while W7-X is LTS). These coils, along with identifying coil numbers assigned for the purpose of this study, are shown in Fig. 4. Note that Fig. 3 used the #3 coil of the HSX configuration.

In order to assess sensitivity to coil size and to estimate the minimum buildable coil size, a uniform geometric scale factor was applied to each of the stellarator configurations shown in Fig. 4. The average coil radius ($\langle r_{coil} \rangle$) for each of these designs is plotted against the

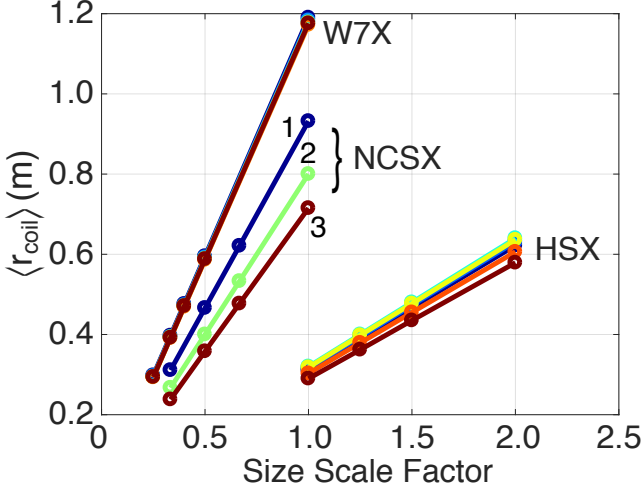


FIG. 5. Mean coil radius ($\langle r_{coil} \rangle$) for each of the stellarator geometries considered as a function of the size scale factor applied. Size scale factor of 1 is the size of the as-built coil.

size scale factor applied in Fig. 5. $\langle r_{coil} \rangle$ is defined here as the mean distance from the coil trajectory to the coil geometric center. The coil geometric center is in turn defined as the mean position of the coil trajectory.

As can be seen, in terms of $\langle r_{coil} \rangle$, W7-X is the largest though NCSX is only modestly smaller. However as can be seen in Fig. 4, the complexity of the NCSX coils is considerably increased due to the more stringent constraints utilized in its optimization (in particular the desire for a tight aspect ratio). The HSX coils are smallest and also the most simple. All devices were scaled such that they occupied an overlapping $\langle r_{coil} \rangle$ range between 0.2 and 0.6 m.

IV. STRAIN OPTIMIZATION AND MINIMUM COIL SIZE

The main objectives of optimizations involving only strain are to provide headroom to further reduce B_{\perp} and to enable the use of progressively wider HTS tape widths (thus increasing the current capacity per turn). Strain-only optimizations also provide a means of determining the minimum buildable size of a NI-HTS coil at fixed tape width regardless of target B_{\perp} . As described in Sec. II A, a value of 0.4% is considered engineering best practice and is here used as the target allowable ϵ_{tot} . Results will be conveyed by plotting the peak strain (ϵ_{tot}) vs coil size ($\langle r_{coil} \rangle$), in case further HTS advances modify the allowable strain.

The full coil trajectory for the #3 HSX coil shown in Fig. 4 (and highlighted in Fig. 3) is shown in Fig. 6. For this coil, some regions of the coil trajectory are very strongly constrained by ϵ_{bend} while others are not. The tensioned spline approach allows quick identification of the optimal θ_{wind} trajectory.

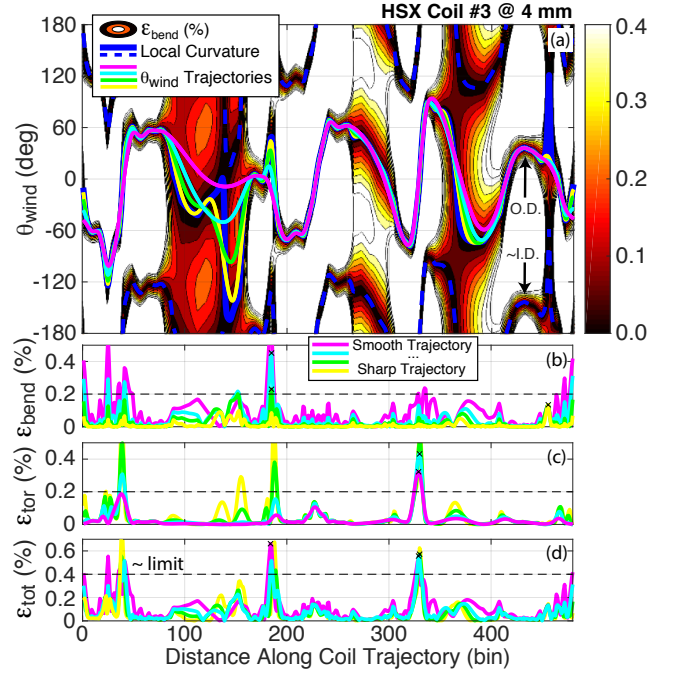


FIG. 6. The same θ_{wind} trajectories of Fig. 3 now displayed for the entire HSX #3 coil trajectory. Again varying the spline tension yields (a) various candidate θ_{wind} trajectories. (b-d) These different trajectories trade off ϵ_{bend} and ϵ_{tor} differently, giving rise to an optimum in the total strain (ϵ_{tot}).

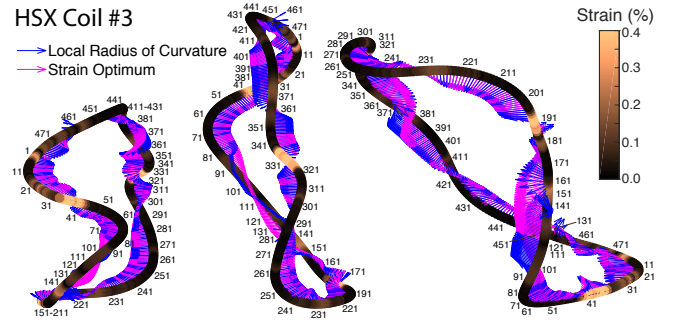


FIG. 7. Three viewing angles of HSX coil #3 showing the local radius of curvature (blue vectors) and optimal θ_{wind} trajectory (magenta vectors) for a strain-only optimization. Colors along the coil trajectory indicate relative ϵ_{tot} . Regions of high ϵ_{tot} are found at the transition between bends.

Figure 7 presents a graphical assessment of the θ_{wind} optimization results and uses the color axis to highlight the regions where the strain is most severe. As can be seen the weak points are in the transition between bends, where some amount of ϵ_{bend} and ϵ_{tor} is unavoidable. Comparing Fig. 6 and Fig. 7, these occur around bins 35, 190, and 330. The winding angle (pink vector in Fig. 7) changes angle by a significant amount at these points, yet there is still a finite bend radius.

The impact of size scale factor on ϵ_{bend} , ϵ_{tor} , and ϵ_{tot} is shown in Fig. 8, again using HSX coil #3. For each size

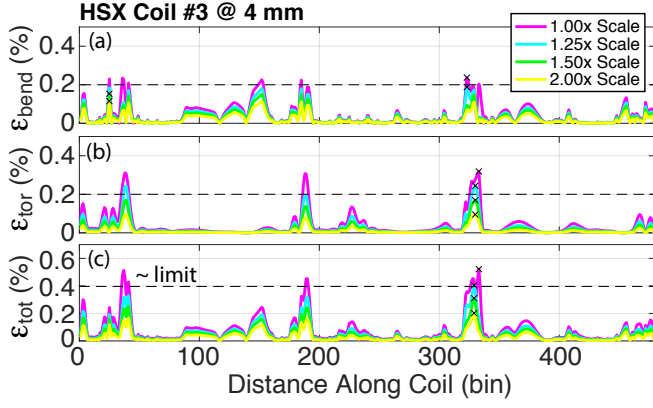


FIG. 8. Variation of the strain components as a function of size scale factor for HSX coil #3. For each size scale factor the trajectory is optimized as in Fig. 6. The maximum ϵ_{tot} (x-marks) naturally decreases with size.

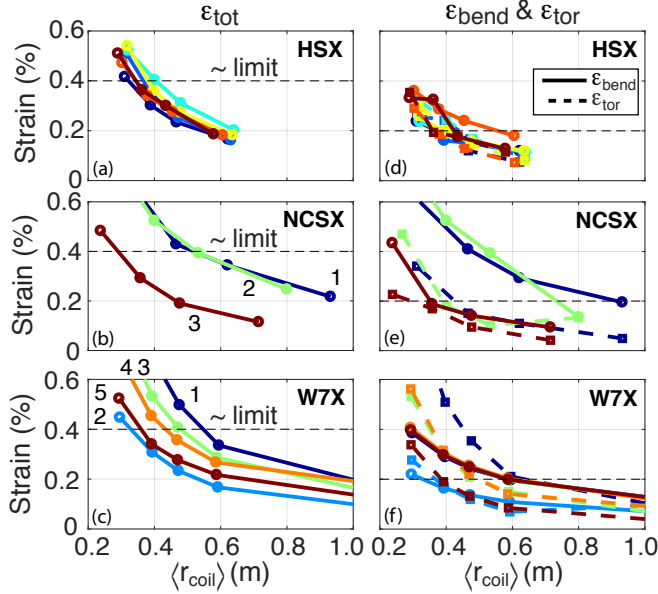


FIG. 9. (a-c) Peak total strain (ϵ_{tot}) and (d-f) peak bending (ϵ_{bend}) and torsion (ϵ_{tor}) strain for the stellarator configurations as a function of average coil size ($\langle r_{coil} \rangle$) for 4 mm wide tape. As $\langle r_{coil} \rangle$ decreases, the target ϵ_{tot} is exceeded, thus defining the minimum $\langle r_{coil} \rangle$.

scale factor, optimization including possible manual intervention as described in Sec. IID has been undertaken. Despite optimization, it is found that the 1.0x size (as-built) coil exceeds the target strain of 0.4%. As such, the as-built HSX is found to be too small to be compatible with the NI-HTS strain limits as here assumed. Increasing the size scale factor naturally reduces the strain, and already by 1.50x scale factor the strain is below the assumed limit.

Using the same methodology, strain assessment as a function of coil size ($\langle r_{coil} \rangle$) was conducted for all coils of the HSX, W7-X, and NCSX stellarators. Results are

presented in Fig. 9. As coil size decreases, the target total strain is exceeded, thus defining the minimum buildable $\langle r_{coil} \rangle$ for these existing configurations. Generally, a minimum $\langle r_{coil} \rangle$ of 0.3 - 0.5 m is found, though variations between coils and configurations exist.

Note that HSX coil #3 is highlighted because it is most severely limited by strain, despite the fact that it is not the most non-planar. This implies the degree of non-planar complexity is not directly related to the strain limits encountered, and further suggests optimization of the coil trajectory itself has the potential to significantly improve compatibility with NI-HTS coils. This is further discussed in Appendix A.

V. COMBINED STRAIN AND TRANSVERSE FIELD OPTIMIZATION

Optimizations considering cost functions involving both strain (ϵ_{bend} , defined in Sec. IIA) and transverse field (B_{\perp} , defined in Sec. IIB) using cost functions defined in Sec. IIC are now presented. Coils optimized for both considerations must be larger than the minimum coil size ($\langle r_{coil} \rangle$) shown in Fig. 9, as headroom in strain is needed to trade-off against other factors (like B_{\perp}). Recall that to compute B_{\perp} the magnetic fields from all the coils comprising the configuration must be taken into account.

Strain only (magenta) and combined strain + B_{\perp} (cyan) optimizations are demonstrated for coil #1 of the W7-X stellarator configuration, with optimized trajectories shown in Fig. 10. For this larger coil the larger radii of curvatures yield ϵ_{bend} contours that are significantly lower [Fig. 10(b)], enabling deviation of θ_{wind} from the ϵ_{bend} minimum. Contours of B_{\perp} [Fig. 10(c)] show a different dependency on θ_{wind} . The combined optimization (cyan lines) follow the cost function target (green) very closely, essentially overlaying. For the combined optimization, ϵ_{tot} now takes a finite value for most of the trajectory [Fig. 10(a)], very close to the input ϵ_0 in Eq. 4 value of 0.2 %. The B_{\perp} value was also meaningfully reduced by this method, by nearly 50%.

At this point it should be mentioned that some coils (such as the one highlighted in Fig. 10) contain apparent artefacts in the coil trajectory that inhibit compatibility with NI-HTS. This can be seen in the wiggles in the local curvature (blue line) in Fig. 10(b) around bin #210. As size scale factor is reduced, this feature imposes a high strain and limits the buildable size. As can be seen in Fig. 11, this artefact occurs at the nominally straight section of the coil. While seemingly straight, these sectors are found to contain finite curvature (and finite ϵ_{bend}) requiring significant torision (ϵ_{tor}) to mitigate. Improved coil trajectory definition should avoid these artefacts as will be described in Appendix A.

Using publicly available data on the achievable I_{crit} for a given HTS tape width at various B_{\perp} and operating temperature conditions²⁶, the HTS tape length needed

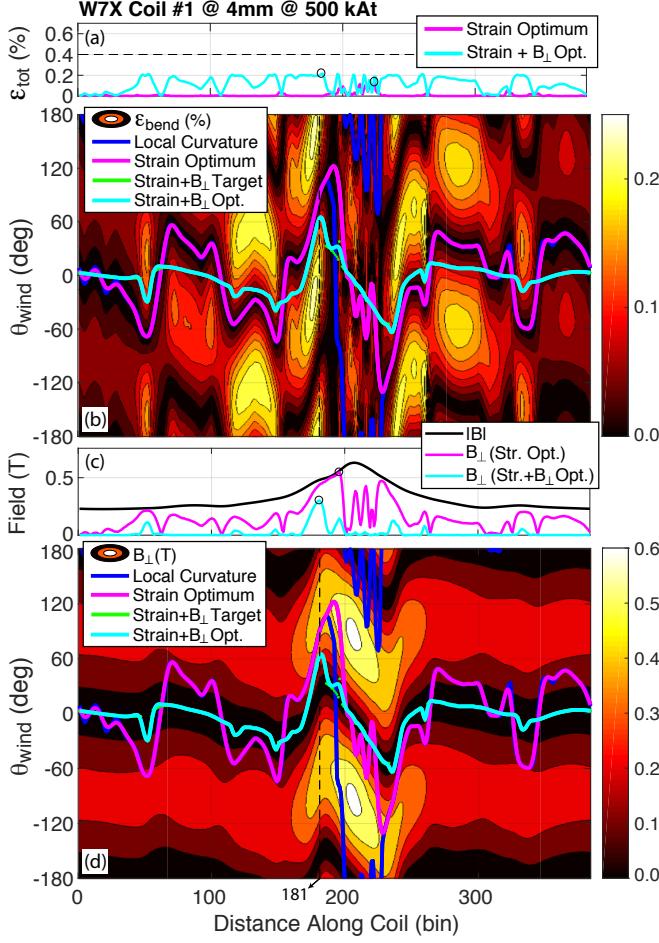


FIG. 10. Comparison of strain only (magenta) and combined strain+ B_{\perp} (cyan) optimization for W7-X coil #1. Evaluations of (a) ϵ_{tot} , (b) ϵ_{bend} vs. θ_{wind} , (c) B_{\perp} and (d) B_{\perp} vs. θ_{wind} . Allowing finite ϵ_{tot} enables a significant reduction of B_{\perp} along the optimal θ_{wind} trajectory.

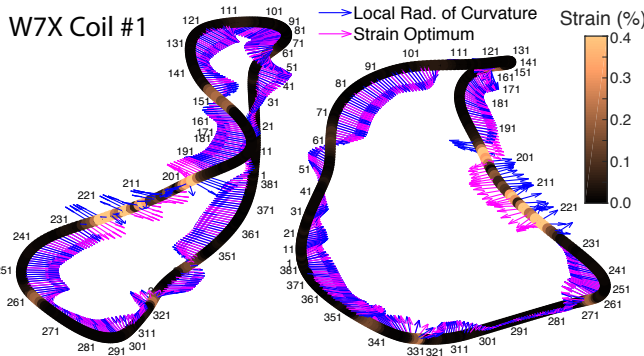


FIG. 11. Two viewing angles of W7-X coil #1 including the local radius of curvature (blue vectors) and optimal θ_{wind} trajectory (magenta vectors) for a strain-only optimization. Colors along the coil trajectory indicate relative ϵ_{tot} . Regions of high ϵ_{tot} are found at the straight section, indicating an artificial constraint is present.

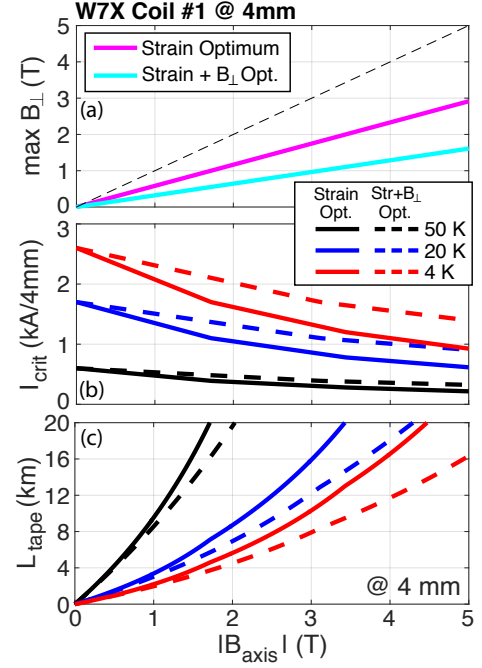


FIG. 12. (a) Transverse field (B_{\perp}), (b) critical current (I_{crit}), and (c) required HTS tape length as a function of B_{axis} for W7-X coil #1.

for a given B_{axis} can be estimated. This is shown in Fig. 12 for the same trajectories of Fig. 10 using W7-X coil #1. The reduction in B_{\perp} enables a meaningful increase in the achievable B_{axis} for fixed tape width (L_{tape}) or alternatively a reduction in L_{tape} for a fixed B_{axis} .

A second example is provided using the same HSX coil #3 described in detail in Sec. IV. However, since the 1x size scale factor was already above the target strain limit, a 2x size scale factor is used. This provides the necessary headroom to in principle optimize against both strain and B_{\perp} . However, as shown in Fig. 13, allowing finite strain does not significantly improve optimization performance, with peak B_{\perp} is nearly unchanged. Looking in detail at the constrained region in Fig. 13(e), the ϵ_{bend} is found to be below ϵ_0 only in a small region of θ_{wind} . Within this allowable θ_{wind} region, no significant B_{\perp} reduction can be achieved. Thus, this particular coil is resistant to further optimization.

Mapping of the I_{crit} data to this coil as B_{axis} is scaled is shown in Fig. 14 for HSX coil #3 at 2x size scale factor. As B_{\perp} did not much change when included in the optimization, both strain only and combined yield similar results. Note this coil (even at 2x size scale factor) requires significantly less L_{tape} to achieve meaningful B_{axis} due to its smaller size as compared to the W7-X coils.

Combined optimization of all the coils in the HSX configuration at 2x size scale factor is performed and results are given in Fig. 15. For many coils, the B_{\perp} component could be meaningfully reduced, especially for the least planar (coils #1, 2). As discussed, the coil #3 was

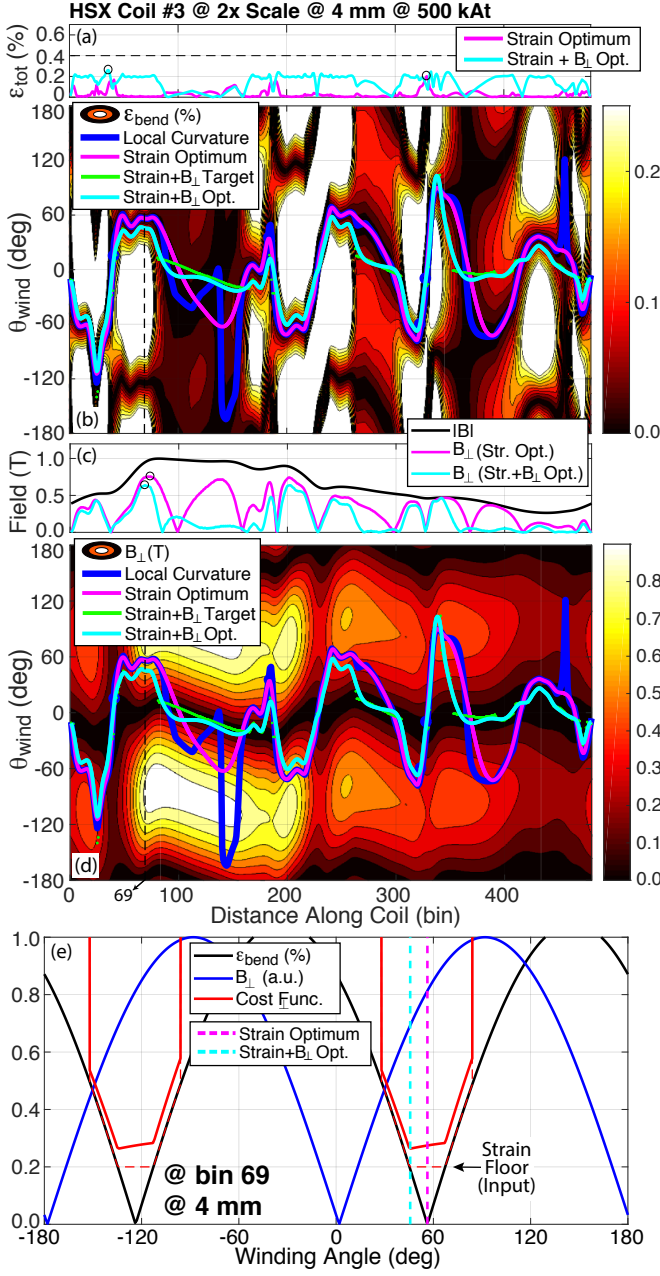


FIG. 13. Comparison of strain only (magenta) and combined strain+ B_{\perp} (cyan) optimization for HSX coil #3 at 2x size scale factor. Evaluations of (a) ϵ_{tot} , (b) ϵ_{bend} vs. θ_{wind} , (c) B_{\perp} and (d) B_{\perp} vs θ_{wind} . Allowing finite ϵ_{tot} is not found to improve this optimization by a significant degree, due to (e) a poor alignment of B_{\perp} and ϵ_{bend} constraints around bin #69.

barely affected, and the other most planar coils less-so. Nonetheless, at least in some instances the increased allowance for strain enables a significant reduction in the needed L_{tape} . Final adjudication between all optimization constraints requires a target B_{axis} as well as a notional budget, as increasing L_{tape} implies an increased cost penalty.

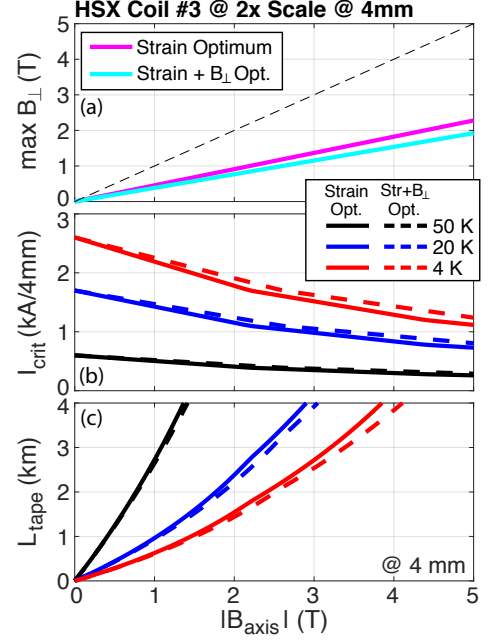


FIG. 14. (a) Transverse field (B_{\perp}), (b) critical current (I_{crit}), and (c) required HTS tape length as a function of B_{axis} for HSX coil #3 at 2x size scale factor. Combined strain + B_{\perp} optimization did not improve the required L_{tape} in this case.

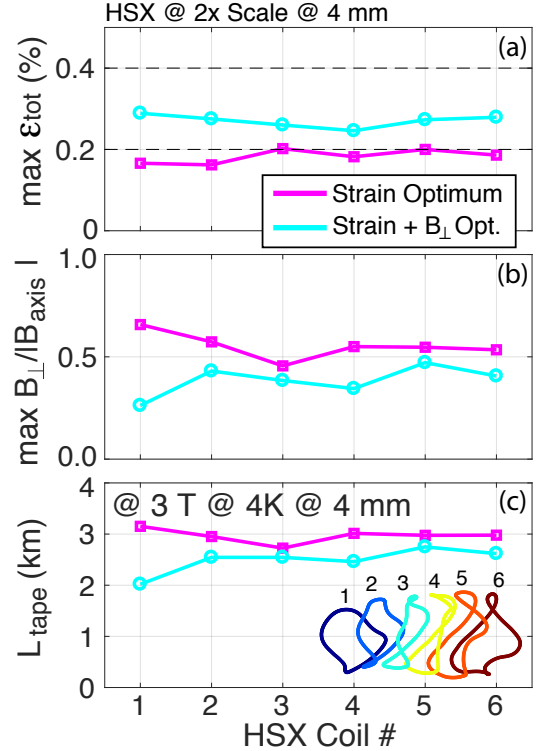


FIG. 15. Summary of performance improvement via combined strain + B_{\perp} optimization for all HSX coils at 2x size scale factor. The most planar coils (#1, 2) obtain a meaningful benefit while the more planar coils are fairly constrained and do not benefit as much. In both optimizations, L_{tape} of a few km gives access to B_{axis} of several T.

VI. DISCUSSION AND CONCLUSIONS

This work has presented the benefits and drawbacks of NI-HTS magnet technology specifically for its application to non-planar coils. A novel winding angle optimization method is introduced to mitigate the drawbacks of increased minor-axis bending strain (ϵ_{bend}), torsional strain (ϵ_{tor}), and increased transverse field (B_{\perp}). By trading off the two strains against each other via an optimized θ_{wind} trajectory, a minimum peak total strain and a reduced B_{\perp} can be obtained. This minimum peak total strain in turn enables assessment of the minimum buildable size for a given input non-planar coil geometry. For well-known existing stellarator designs, the minimum size was found to be 0.3 - 0.5 m for 4 mm wide HTS tape. For coils larger than this minimum size, the total strain (ϵ_{tot}) can be traded off against B_{\perp} to reduce this component. This enables a reduction of the length of HTS tape required to achieve a given design magnetic field or equivalently an increase in the achievable magnetic field for constant HTS tape length.

Appendix A: Optimization of the Coil Trajectory for Stellarator Applications

This work has focused on optimizing the winding angle optimization of a pre-defined coil to maximize compatibility with NI-HTS magnet technology. Considerations for optimizing the coil trajectory itself now are briefly summarized. This discussion focuses on stellarator applications, as there are many possible degrees of freedom in the coil geometry of these concepts and significant coil optimization work already exists in this area^{32–38}.

Stellarator coil optimizations are done with many constraints in mind, most having to do with plasma physics. Considering the constraints arising from the coil technology itself, two constraints are usually included: curvature and coil-coil distance. Interestingly, NI-HTS magnets pose significantly different constraints than conventionally considered.

First, considering curvature, for a NI-HTS magnet strain arising from regular curvature is negligible, and is also called ‘major-axis’ bending. The strain issues discussed in Sec. IV are important, and in particular the interplay of torsion and wrong-ways bending. If curvature is weakly penalized, yet torsion is not, very different stellarator coil shapes may arise from optimizations against these alternate criteria, particularly with more pronounced toroidal joggles.

Second, considering coil-coil spacing, the compactness (high current density) and mechanical strength (steel substrate and bobbin) inherent to the NI-HTS magnet has the potential to support significantly reduced coil-coil spacing. The final spacing depends the amount of bobbin material required, which arises from the electromagnetic forces, which require definition of the target operating magnetic field. However, at least as compared to copper

and LTS, significantly smaller coil-coil separations can be anticipated.

Finally, stellarator coils are usually parametrized via Fourier series. As for example in the W7-X coil of Fig. 11, this gives rise to an artefact in the straight sections of the coil where residual undulations exist from incomplete cancellation of the Fourier series. These residual undulations severely compromise compatibility with NI-HTS, despite their origin from a mostly-straight section of the coil. Using tensioned splines to parametrize the coil trajectory should remove this artificial limitation.

While outside the scope of this activity, stellarator coil optimizations using these alternate criteria are thus highlighted as fertile ground for future study.

ACKNOWLEDGMENTS

This work was supported by General Atomics Internal Funds. The author would like to thank A. Benson, B. Breneman, J. Leuer, J. Smith, Z.B. Piec, and L. Holland for useful discussions. The author also thanks S. Lazerson and A. Bader for the provision of the existing stellarator device coil geometry information.

- ¹Bruzzone P, Fietz W H and Minervini J V 2018 *Nucl. Fusion* **58** 103001 URL <https://doi.org/10.1088/1741-4326/aad835>
- ²Haught D, Daley J, Bakke P and Marchionini B 2007 *International Journal of Applied Ceramic Technology* **4** 197–202 ISSN 1546542X URL <https://doi.org/10.1111/j.1744-7402.2007.02133.x>
- ³Fietz W H, Barth C, Drotziger S, Goldacker W, Heller R, Schlachter S I and Weiss K P 2013 *Fusion Engineering and Design* **88** 440–445 ISSN 09203796 URL <http://dx.doi.org/10.1016/j.fusengdes.2013.03.059>
- ⁴Whyte D G, Minervini J, LaBombard B, Marmar E, Bromberg L and Greenwald M 2016 *Journal of Fusion Energy* **35** 41–53 ISSN 01640313 URL <https://doi.org/10.1007/s10894-015-0050-1>
- ⁵Maingi R, Lumsdaine A, Allain J P, Chacon L, Gourlay S A, Greenfield C M, Hughes J W, Humphreys D, Izzo V, McLean H, Menard J E, Merrill B, Rapp J, Schmitz O, Spadaccini C, Wang Z, White A E and Wirth B D 2019 *Fusion Science and Technology* **75** 167–177 ISSN 19437641 URL <https://doi.org/10.1080/15361055.2019.1565912>
- ⁶Sorbom B N, Ball J, Palmer T R, Mangiarotti F J, Sierchio J M, Bonoli P, Kasten C, Sutherland D A, Barnard H S, Haakonsen C B, Goh J, Sung C and Whyte D G 2015 *Fusion Engineering and Design* **100** 378–405 ISSN 09203796 (Preprint 1409.3540) URL <http://dx.doi.org/10.1016/j.fusengdes.2015.07.008>
- ⁷Sykes A, Costley A E, Windsor C G, Asunta O, Brittles G, Buxton P, Chuyanov V, Connor J W, Gryaznevich M P, Huang B, Hugill J, Kukushkin A, Kingham D, Langtry A V, McNamara S, Morgan J G, Noonan P, Ross J S, Shevchenko V, Slade R and Smith G 2018 *Nuclear Fusion* **58** ISSN 17414326 URL <https://doi.org/10.1088/1741-4326/aa8c8d>
- ⁸Miura Y, Sakota M and Shimada R 1994 *IEEE Transactions on Magnetics* **30** 2573–2576 ISSN 19410069 URL <https://doi.org/10.1109/20.305804>
- ⁹Thomas C M, Faircloth D C and Jago S J 2005 *Proceedings of the IEEE Particle Accelerator Conference* **2005** 1652–1654 URL <https://doi.org/10.1109/PAC.2005.1590866>
- ¹⁰Amemiya N, Miyahara H, Ogitsu T and Kurusu T 2015 *Physics Procedia* **67** 776–780 ISSN 18753892 URL <http://dx.doi.org/10.1016/j.phpro.2015.06.131>

- ¹¹Najmabadi F and Raffray A R 2006 *Fusion Engineering and Design* **81** 2679–2693 ISSN 09203796 URL <https://doi.org/10.1016/j.fusengdes.2006.07.087>
- ¹²Wolf R C 2008 *Fusion Engineering and Design* **83** 990–996 ISSN 09203796 URL <https://doi.org/10.1016/j.fusengdes.2008.05.008>
- ¹³Goldacker W, Frank A, Heller R, Schlachter S I, Ringsdorf B, Weiss K P, Schmidt C and Schuller S 2007 *IEEE Transactions on Applied Superconductivity* **17** 3398–3401 ISSN 10518223 URL <https://doi.org/10.1109/TASC.2007.899417>
- ¹⁴Weiss J D, Mulder T, Ten Kate H J and Van Der Laan D C 2017 *Superconductor Science and Technology* **30** ISSN 13616668 URL <https://doi.org/10.1088/0953-2048/30/1/014002>
- ¹⁵Takayasu M, Chiesa L, Bromberg L and Minervini J V 2012 *Superconductor Science and Technology* **25** ISSN 09532048 URL <https://doi.org/10.1088/0953-2048/25/1/014011>
- ¹⁶Hahn S, Park D K, Bascuán J and Iwasa Y 2011 *IEEE Transactions on Applied Superconductivity* **21** 1592–1595 ISSN 10518223 URL <https://doi.org/10.1109/TASC.2010.2093492>
- ¹⁷Kim Y G, Hahn S, Kim K L, Kwon O J and Lee H 2012 *IEEE Transactions on Applied Superconductivity* **22** ISSN 10518223 URL <https://doi.org/10.1109/TASC.2011.2181931>
- ¹⁸Hahn S, Radcliff K, Kim K, Kim S, Hu X, Kim K, Abraimov D V and Jaroszynski J 2016 *Superconductor Science and Technology* **29** 1–6 ISSN 13616668 URL <https://doi.org/10.1088/0953-2048/29/10/105017>
- ¹⁹Takayasu M, Minervini J V and Bromberg L 2010 *AIP Conference Proceedings* **1219** 337–344 URL <https://doi.org/10.1063/1.3402320>
- ²⁰Wang X, Arbelaez D, Caspi S, Prestemon S O, Sabbi G L and Shen T 2017 *IEEE Transactions on Applied Superconductivity* **27** ISSN 10518223 URL <https://doi.org/10.1109/TASC.2017.2766132>
- ²¹Gray A, Abbena E and Salamon S 2006 *Modern Differential Geometry of Curves and Surfaces with Mathematica* 3rd ed (Chapman and Hall/CRC) ISBN 9781584884484
- ²²Roark R J, Young W C and Plunkett R 1976 *Formulas for Stress and Strain* 8th ed vol 43 (McGraw-Hill Education) ISBN 0071742476
- ²³Takayasu M and Chiesa L 2015 *IOP Conference Series: Materials Science and Engineering* **102** 012023 ISSN 1757899X URL <https://doi.org/10.1088/1757-899X/102/1/012023>
- ²⁴Allen N C, Chiesa L and Takayasu M 2015 *IEEE Transactions on Applied Superconductivity* **25** 1–5 ISSN 10518223 URL <https://doi.org/10.1109/TASC.2014.2364401>
- ²⁵Zhang Y, Hazelton D W, Kelley R, Kasahara M, Nakasaki R, Sakamoto H and Polyanskii A 2016 *IEEE Transactions on Applied Superconductivity* **26** 8400406 ISSN 10518223 URL <https://doi.org/10.1109/TASC.2016.2515988>
- ²⁶Incorporated S SuperPower Technical Documents URL <http://www.superpower-inc.com/content/technical-documents>
- ²⁷Anderson F S B, Almagri A F, Anderson D T, Matthews P G, Talmadge J N and Shohet J L 1995 *Fusion Technology* **27** 273–277 ISSN 0748-1896 URL <https://doi.org/10.13182/fst95-a11947086>
- ²⁸Beidler C, Grieger G, Herrnegger F, Harmeyer E, Kisslinger J, Lotz W, Maassberg H, Merkel P, Nuehrenberg J, Rau F, Sapper J, Sardei F, Scardovelli R, Schlueter A and Wobig H 1990 *Fusion Technology* **17** 148–168 ISSN 07481896 URL <https://doi.org/10.13182/FST90-A29178>
- ²⁹Klinger T, Baylard C, Beidler C D, Boscary J, Bosch H S, Dinklage A, Hartmann D, Helander P, Maßberg H, Peacock A, Pedersen T S, Rummel T, Schauer F, Wegener L and Wolf R 2013 *Fusion Engineering and Design* **88** 461–465 ISSN 09203796 URL <http://dx.doi.org/10.1016/j.fusengdes.2013.02.153>
- ³⁰Chrzanowski J H, Meighan T, Raftopoulos S, Fogarty P J, Heitzenroeder P J, Nelson B and Williamson D 2007 *Proceedings - Symposium on Fusion Engineering* URL <https://doi.org/10.1109/FUSION.2007.4337903>
- ³¹Zarnstorff M C, Berry L A, Brooks A, Fredrickson E D, Fu G Y, Hirshman S P, Hudson S R, Ku L P, Lazarus E A, Mikkelsen D, Monticello D, Neilson G H, Pomphrey N, Reiman A H, Spong D A, Strickler D J, Boozer A H, Cooper W A, Goldston R J and Hatcher R E 2001 *Plasma Phys. Control. Fusion* **43** A237 URL <https://doi.org/10.1088/0741-3335/43/12A/318>
- ³²Merkel P 1987 *Nuclear Fusion* **27** 867–871 ISSN 17414326 URL <https://doi.org/10.1088/0029-5515/27/5/018>
- ³³Pomphrey N, Berry L, Boozer A, Brooks A, Hatcher R E, Hirshman S P, Ku L P, Miner W H, Mynick H E, Reiersen W, Strickler D J and Valanju P M 2001 *Nuclear Fusion* **41** 339–347 ISSN 00295515 URL <https://doi.org/10.1088/0029-5515/41/3/312>
- ³⁴Strickler D J, Berry L A and Hirshman S P 2002 *Fusion Science and Technology* **41** 107–115 ISSN 1536-1055 URL <https://doi.org/10.13182/fst02-a206>
- ³⁵Zhu C, Hudson S R, Song Y and Wan Y 2018 *Nuclear Fusion* **58** 016008 ISSN 17414326 URL <https://doi.org/10.1088/1741-4326/aa8e0a>
- ³⁶Zhu C, Hudson S R, Song Y and Wan Y 2018 *Plasma Physics and Controlled Fusion* **60** 065008 ISSN 13616587 URL <https://doi.org/10.1088/1361-6587/aab8c2>
- ³⁷Landreman M 2017 *Nuclear Fusion* **57** 046003 ISSN 17414326 URL <https://doi.org/10.1088/1741-4326/aa57d4>
- ³⁸Paul E J, Landreman M, Bader A and Dorland W 2018 *Nuclear Fusion* **58** ISSN 17414326 URL <https://doi.org/10.1088/1741-4326/aac1c7>